RSC Advances

PAPER

View Article Online
View Journal | View Issue



Check for updates

Cite this: *RSC Adv.*, 2024, **14**, 7999

# Three-dimensional NiCoS nanotubes@NiCo-LDH nanosheets core–shell heterostructure for high-rate capability alkaline zinc-based batteries†

Linxi Dai, Shangshu Peng, Xinhai Wang, Bo Chen, Yang Wu, Quan Xie and Yunjun Ruan *

Received 20th January 2024
Accepted 4th March 2024

DOI: 10.1039/d4ra00521j

rsc.li/rsc-advances

Aqueous alkaline zinc-based batteries (AAZBs) are promising for large-scale applications due to their high working voltage, safety, and low cost. However, the further development of AAZBs has been significantly hindered by the low electronic conductivity and poor cycling stability of traditional nickel/cobalt-based cathode materials. In this work, a binder-free electrode was successfully designed by electrodepositing NiCo-LDH nanosheets on NiCoS nanotube arrays that were grown on nickel foam (NiCoS@NiCo-LDH). The unique three-dimensional core–shell heterostructures not only enhance electrical conductivity but also offer abundant active sites and rapid ion/electron transport channels, thereby improving its electrochemical performance. The as-fabricated NiCoS@NiCo-LDH electrode delivers a capacity of 312 mA h $g^{-1}$ (0.624 mA h $cm^{-2}$) at 2 mA $cm^{-2}$ and exhibits high rate capability with 90% capacity retention at 10 mA $cm^{-2}$. Additionally, the assembled NiCoS@NiCo-LDH//Zn battery exhibits a high energy density of 435.3 W h $kg^{-1}$ at a power density of 4.1 kW $kg^{-1}$ and maintains 95.9% of its capacity after 3000 cycles at a current density of 20 mA $cm^{-2}$.

## 1 Introduction

As the world rapidly depletes its traditional fossil fuel reserves, the demand for green and sustainable energy sources is increasingly growing.[1–3] Rechargeable batteries, serving as an effective energy storage technology, are being extensively researched and applied in large-scale energy storage.[4–6] Among these, lithium-ion batteries dominate in a wide range of applications, such as portable electronics and electric vehicles, due to their exceptionally high energy density and good cycle durability.[7–9] However, the scarcity of lithium resources leads to high production costs, and the safety issues associated with toxic and flammable organic electrolytes limit their further development.[10,11] Consequently, aqueous electrolytes are considered a more promising alternative from economic and safety perspectives.[12–14] Among various aqueous rechargeable batteries, aqueous alkaline zinc-based batteries (AAZBs) show promising potential for large-scale energy storage due to their high operating voltage, safety, the high theoretical capacity of the zinc anode (820 mA h $g^{-1}$), an abundance of zinc resources, and environmental friendliness.[15–19]

To date, novel nickel-based cathode materials with various morphological structures and compositions have been developed for aqueous alkaline zinc-based batteries, such as $Ni(OH)_2$,[20,21] NiO,[22] $NiCo_2O_4$,[23] NiCo-DH,[24] $NiSe_2$ (ref. 25) and $Ni_3S_2$.[26] However, compared with the advantages of zinc anodes, conventional nickel-based cathode materials have disadvantages such as low electronic conductivity and poor cycling stability. To solve the above problems, a large number of strategies including doping, surface modification, the introduction of defects, and structural design have been explored. The doping of heteroatoms can regulate the electrical conductivity of electrode materials and promote the reaction kinetic process to obtain excellent electrochemical properties.[27,28] Li *et al.* proposed a strategy of F doping into cobalt–nickel hydroxides, which produced good micro-morphology and phase structure features and enhanced the electronegativity of hydroxides.[29] Compared with pristine NiCo–CH, the fluorine-doped NiCo–CH (NiCo–CH–F) exhibits excellent multiplicity performance (66% retention at 8 A $g^{-1}$) and cycling stability (capacity retention after 10 000 cycles over 90%). Secondly, conductive coating on the surface of electrode materials can improve surface reactivity and reaction kinetics. Zhou *et al.* prepared nickel–cobalt phosphate octahydrate electrodes by a one-step hydrothermal process, whose capacity retention was increased to 98.31% from the previous 58.59% after surface-coating with carbon materials.[30] Thirdly, defects can enhance the interaction between the electrode material and ions in the electrolyte, and accelerate the surface reactivity and reaction

*Institute of Advanced Optoelectronic Materials and Technology, College of Big Data and Information Engineering, Guizhou University, Guiyang 550025, China. E-mail: yjruan@gzu.edu.cn*

† Electronic supplementary information (ESI) available. See DOI: https://doi.org/10.1039/d4ra00521j

kinetics of the electrode material.[31] Yao *et al. in situ* introduced oxygen-vacancy-enriched $CoNiO_2$ nanosheets on the surface of vertical Ni nanotubes (Od-CNO@Ni NTs), where the introduction of oxygen vacancies enhanced the adsorption energy of $OH^-$ ions and the stability of the crystalline structure of the battery in the cycles.[32] The assembled Od-CNO@Ni NTs//Zn rechargeable battery exhibits an energy density of 547.5 W h $kg^{-1}$ at a power density of 92.9 kW $kg^{-1}$ and maintains 93.0% capacity after 5000 cycles. Fourthly, proper structural design enables cathode materials to increase the specific surface area and expose more active sites, such as nanotubes, nanosheets, and nanofibres. Fei *et al.* synthesized a sugar gourd-like yolk–shell Ni–Mo–Co–S nanocage arrays on nickel foam, exhibiting a high areal capacity of 1.96 mA h $cm^{-2}$ and excellent cycling stability at a current density of 5 mA $cm^{-2}$.[33] Cui *et al.* employed electrospinning to synthesize carbon nanofibers functionalized with $NiCo_2S_4$ nanoparticles (CNF@$NiCo_2S_4$).[34] The fabricated CNF@$NiCo_2S_4$//Zn batteries demonstrated high capacities of 0.32 mA h $cm^{-2}$ and 35.9 mA h $cm^{-3}$ at a current density of 2 mA $cm^{-2}$. To further enhance electrode capacity, hierarchical structures have been constructed to provide additional redox-active sites, enriching ion diffusion and electron transport pathways. The formation of composite structures combines the advantages of each component, exhibiting unique synergistic effects that significantly enhance the specific capacity and rate performance of electrode materials.[35] Shi *et al.* increased the capacity of a layered Mo–$NiS_2$@NiCo-LDH electrode from 207.9 mA h $g^{-1}$ (for Mo–$NiS_2$) to 325.6 mA h $g^{-1}$ (at 1 A $g^{-1}$) by decorating Mo–$NiS_2$ flakes with NiCo layered double hydroxide (NiCo-LDH) nanosheets.[36]

Herein, we introduce a novel cathode material for AAZBs: a binder-free 3d NiCoS nanotubes@NiCo-LDH nanosheets (NiCoS@NiCo-LDH) heterostructures on nickel foam. Typically, it involved a two-step hydrothermal method for synthesizing NiCoS nanotubes directly onto nickel foam, followed by a constant potential electrodeposition process to grow ultrathin NiCo-LDH nanosheets on these nanotubes uniformly. The as-prepared three-dimensional core–shell heterostructure optimizes electrical conductivity and offers many active sites alongside rapid pathways for ion and electron transport. These enhancements in structural and functional properties have led to a notable improvement in electrochemical performance. Our work explores the potential of the novel NiCoS@NiCo-LDH cathode material in enhancing the performance and durability of AAZBs, paving the way for their broader application in sustainable energy storage solutions.

# 2 Experimental sections

## 2.1 Synthesis of NiCoS nanotubes

Before the synthesis, the nickel foam was ultrasonically cleaned for 15 min sequentially in 3 M hydrochloric acid, ethanol, and deionized water. In the typical synthesis process, 4 mmol of $Co(NO_3)_2 \cdot 6H_2O$, 2 mmol of $NiCl_2 \cdot 6H_2O$, 1 mmol of cetyltrimethylammonium bromide (CTAB), and 15 mmol of urea were dissolved in 60 mL of deionized water, stirred for 20 min to form a transparent pink solution. This solution was then transferred to a 100 mL stainless steel autoclave lined with polytetrafluoroethylene (PTFE), and the pre-cleaned nickel foam was inserted. The reaction was maintained at 120 °C for 6 h. Upon cooling to room temperature, the product was thoroughly rinsed several times with deionized water and anhydrous ethanol and then air-dried to obtain the Ni–Co precursor. Subsequently, the nickel foam with the Ni–Co precursor was placed in a solution containing 60 mL of 0.03 M sodium sulfide, transferred to a 100 mL PTFE-lined stainless steel autoclave, and reacted at 120 °C for 6 h. After cooling to room temperature, the nickel foam was washed several times with deionized water and ethanol and then dried in a vacuum oven at 60 °C for 6 h. The mass of NiCoS on the nickel foam was approximately 1.76 mg $cm^{-2}$.

## 2.2 Synthesis of NiCoS@NiCo-LDH

20 mM of $Co(NO_3)_2 \cdot 6H_2O$ and 40 mM of $Ni(NO_3)_2 \cdot 6H_2O$ were mixed to prepare the electrodeposition electrolyte. The nickel foam with NiCoS nanotubes was used as the working electrode, with platinum foil and Hg/HgO electrodes serving as the counter and reference electrodes, respectively. Electrodeposition was carried out at a voltage of −0.9 V for 120 s, then rinsing with deionized water and drying. The mass of NiCoS@NiCo-LDH on the nickel foam was approximately 2.00 mg $cm^{-2}$. A similar method was employed to electrodeposit NiCo-LDH nanosheets on a pure nickel foam substrate, resulting in a loading mass of about 0.20 mg $cm^{-2}$.

## 2.3 Material characterization

X-ray diffraction (XRD, PANalytical Empyrean) was employed to determine the phase composition and crystallinity of the samples. The microstructure of the materials was analyzed using scanning electron microscopy (SEM, Hitachi SU8010). Transmission electron microscopy (TEM, JEOL JEM-F200) was utilized to observe the microscopic structure and lattice fringes of the materials and to ascertain the elemental distribution within the samples. X-ray photoelectron spectroscopy (XPS, Thermo Scientific ESCALAB $Xi^+$) was conducted to analyze the valence states and chemical structure of elements on the sample surfaces.

## 2.4 Electrochemical measurement

Electrochemical measurements, including cyclic voltammetry (CV), galvanostatic charge–discharge (GCD), and electrochemical impedance spectroscopy (EIS), were conducted using an electrochemical workstation (CHI760E). Rate performance and cycle life were measured using a NEWARE battery testing system. In the three-electrode configuration, a 6 M KOH solution was used as the electrolyte. The nickel foam with the active material served as the working electrode, with the Hg/HgO electrode as the reference electrode and the platinum (Pt) electrode as the counter electrode. A coin cell was assembled using NiCoS@NiCo-LDH as the cathode and commercial zinc foil as the anode, with an electrolyte of 6 M KOH containing saturated ZnO. All electrochemical experiments were carried

 

out at room temperature. The specific capacity was calculated using the following equations:

$$C_m = \frac{I \times \Delta t}{m} \quad (1)$$

$$C_s = \frac{I \times \Delta t}{A} \quad (2)$$

where $C_m$ is the mass capacity (mA h $g^{-1}$), $C_s$ is the areal capacity (mA h $cm^{-2}$), $I$ is the discharge current (A), $\Delta t$ is the discharge time (h), $m$ is the mass of the active material (g), and $A$ is the area of the electrode ($cm^{-2}$).

The energy density ($E$, W h $kg^{-1}$) and power density ($P$, kW $kg^{-1}$) are calculated using the following equations:

$$E = C_m \times \Delta V \quad (3)$$

$$P = \frac{3.6 \times E}{\Delta t} \quad (4)$$

## 3 Results and discussion

As illustrated in Fig. 1, the binder-free NiCoS@NiCo-LDH cathode was synthesized using a combination of hydrothermal and electrodeposition methods. Initially, a well-arranged array of NiCo precursor nanorods was grown on nickel foam *via* a simple hydrothermal process. In the second step, uniformly NiCoS nanotubes were grown through hydrothermal sulfidation. Finally, NiCo-LDH nanosheets were uniformly formed on the surface of the NiCoS nanotubes *via* a constant potential electrodeposition technique, resulting in a unique three-dimensional core–shell heterostructure.

The microstructure of the samples was examined using SEM. As shown in Fig. S1a (see the ESI†), the pure nickel foam substrate exhibits a smooth surface with a three-dimensional mesh-like structure. Nickel–cobalt precursor nanorods were grown on the nickel foam using a hydrothermal reaction. After a secondary hydrothermal sulfidation process, the nickel–cobalt precursors transformed into a dense and uniformly arranged array of NiCoS nanotubes, as depicted in Fig. 2a. Fig. 2b and c illustrate the successful growth of ultra-thin and uniform NiCo-LDH nanosheets on the surface of NiCoS nanotubes through constant potential electrodeposition. Similarly, pure NiCo-LDH nanosheets were synthesized on nickel foam using a comparable method. As shown in Fig. S1b,† the NiCo-LDH nanosheets vertically grew on the nickel foam substrate, forming a network-like structure.

As shown in Fig. 2d, the NiCoS nanotubes have an approximate diameter of 170 nm, and the ultra-thin NiCo-LDH nanosheets are firmly grown on the walls of the NiCoS nanotubes. The high-resolution TEM (HRTEM) image in Fig. 2e reveals that lattice fringe spacings of 0.285 and 0.332 nm correspond to the (311) and (220) planes of $NiCo_2S_4$, while spacings of 0.199 and 0.268 nm are attributed to the (018) and (101) planes of NiCo-LDH, respectively. These observations are in accordance with the diffraction rings observed in the Selected Area Electron Diffraction (SAED) pattern (Fig. 2f). Furthermore, elemental mapping images (Fig. 2g) show a uniform distribution of Ni, Co, S, and O across the nanotubes, further confirming the successful construction of the NiCoS@NiCo-LDH core–shell heterostructure.

Fig. 3a presents the XRD patterns for NiCo-LDH, NiCoS, and NiCoS@NiCo-LDH. The diffraction peaks at 31.5°, 38.3°, 50.5°, and 55.3° correspond to the (311), (400), (511), and (440) planes of cubic $NiCo_2S_4$ (JCPDS no. 20-0782).[37] Weak peaks located at 11.3° and 61.2° can be attributed to the (003) and (113) planes of the hydrotalcite structure in $Ni(OH)_2 \cdot 0.75H_2O$ (JCPDS no. 38-0715).[38] Additionally, the diffraction peak at 21.5° corresponds to the (101) plane of $Ni_{3-x}S_2$ (JCPDS no. 14-0358),[39] while the peaks at 15.4° and 29.8° are associated with the (111) and (311) planes of $Co_9S_8$ (JCPDS no. 86-2273).[40] In Fig. 3b of Raman spectra, the distinguishing peaks of NiCoS at 150, 309, and 352 $cm^{-1}$ are assigned to asymmetric bending of S–$Ni_{tetra}$–S bonds, while the peak at 243 $cm^{-1}$ is attributed to the $E_g$ bending mode of S–$Ni_{tetra}$–S bonds.[41] After electrodeposition of NiCo-LDH nanosheets on the surface of NiCoS nanotubes, the peak at 150 $cm^{-1}$ for the NiCoS@NiCo-LDH vanished. It is possible that the NiCo-LDH coating has led to partial shielding of the S–$Ni_{tetra}$–S bond vibrational modes.[42]

The composition and chemical states of the prepared samples were further analyzed using XPS. As shown in Fig. 3c, the survey spectrum of NiCoS@NiCo-LDH exhibits peaks corresponding to Ni, S, O, and Co elements, consistent with the elemental mapping results (Fig. 2g). The Ni 2p spectrum, shown

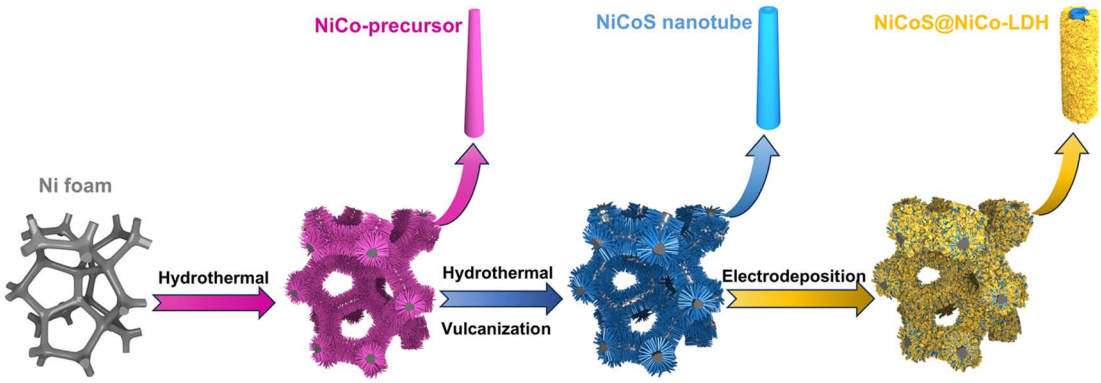


Fig. 1 Schematic diagram of the synthesis of NiCoS@NiCo-LDH.

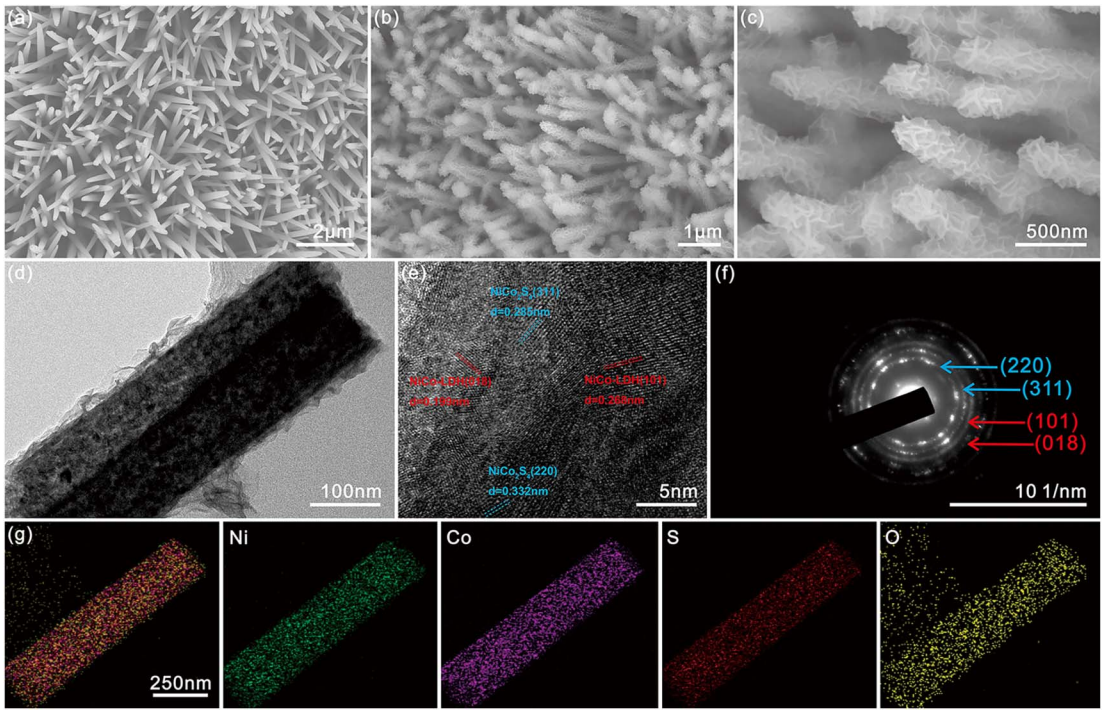


Fig. 2 (a) SEM image of NiCoS. SEM images at (b) low and (c) high magnifications, (d) TEM, (e) HRTEM, (f) SAED pattern, and (g) elemental mappings of NiCoS@NiCo-LDH.

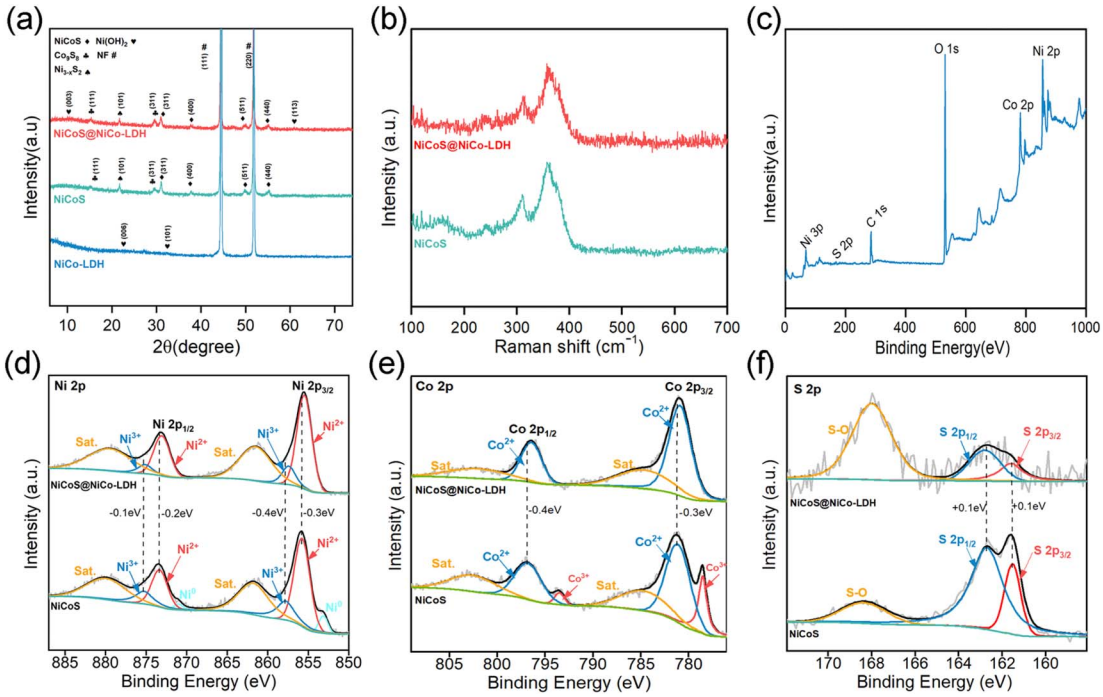


Fig. 3 (a) XRD patterns. (b) Raman patterns. (c) XPS survey spectrum of NiCoS@NiCo-LDH. XPS spectra of (d) Ni 2p, (e) Co 2p, and (f) S 2p for NiCoS@NiCo-LDH and NiCoS.

in Fig. 3d, indicates that the Ni 2p of NiCoS@NiCo-LDH can be well-fitted with two pairs of spin–orbit doublets and two shakeup satellite peaks (sat.). The two characteristic peaks at 857.5 and 875.2 eV are attributed to $Ni^{3+}$, while those at 855.5 and 873.1 eV are attributed to $Ni^{2+}$.[43] The satellite peaks are located at 879.7 and 861.5 eV. For NiCoS, the two peaks at 855.8 and 873.3 eV correspond to $Ni^{2+}$, while those at 857.9 and 875.3 eV correspond to $Ni^{3+}$. The characteristic peaks at 871.0

 

and 853.1 eV originate from metallic nickel in the foam.[48] Compared to NiCoS, the binding energy of Ni $2p_{3/2}$ and Ni $2p_{1/2}$ in NiCoS@NiCo-LDH shows an overall negative shift, indicating an increased electron density around Ni atoms, suggesting chemical bonding between NiCoS nanotubes and NiCo-LDH nanosheets. In the Co 2p spectrum (Fig. 3e), the two peaks at 781.0 and 796.5 eV in NiCoS@NiCo-LDH are assigned to $Co^{2+}$. In NiCoS, the peaks at 781.3 and 796.9 eV correspond to $Co^{2+}$, while the characteristic peaks at 778.6 and 793.5 eV correspond to $Co^{3+}$.[49] Compared to NiCoS, the $Co^{3+}$ $2p_{3/2}$ and $2p_{1/2}$ peaks almost disappear in NiCoS@NiCo-LDH, indicating a predominance of $Co^{2+}$ in NiCo-LDH. Furthermore, for the S 2p spectrum (Fig. 3f), NiCoS@NiCo-LDH shows two peaks at 161.6 (S $2p_{3/2}$) and 162.8 eV (S $2p_{1/2}$), which are shifted positively by 0.1 eV compared to the two peaks at 161.5 (S $2p_{3/2}$) and 162.7 eV (S $2p_{1/2}$) in NiCoS. Peaks at 168.0 and 168.4 eV correspond to oxidized sulfur species due to surface oxidation.[50]

The electrochemical performance of the fabricated electrodes was investigated in a three-electrode system containing 6 M KOH electrolyte. Fig. 4a displays the CV curves of NiCoS@NiCo-LDH, NiCoS, and NiCo-LDH, collected at a scan rate of 5 mV $s^{-1}$ over a potential range of 0 to 0.55 V. Notably, the NiCoS@NiCo-LDH electrode exhibits the highest response current and the largest CV scan area, indicating superior electrochemical activity and charge storage capacity. The CV curves of the NiCoS@NiCo-LDH electrode at scan rates from 1 to 5 mV $s^{-1}$ (Fig. 4b) show distinct symmetrical redox peaks with an increasing current response as the scan rate increases. It demonstrates the typical reversible faradaic redox behavior of the NiCoS@NiCo-LDH electrode during the charge storage process.

Fig. 4c compares the galvanostatic charge–discharge (GCD) curves of NiCoS@NiCo-LDH, NiCoS, and NiCo-LDH electrodes at a current density of 2 mA $cm^{-2}$. The NiCoS@NiCo-LDH electrode demonstrates a notably high areal capacity of 0.624 mA h $cm^{-2}$, substantially surpassing that of the NiCoS electrode (0.378 mA h $cm^{-2}$) and the NiCo-LDH electrode (0.03 mA h $cm^{-2}$). The superior performance is attributed to the synergistic effect exhibited by the core–shell heterostructure of NiCoS@NiCo-LDH, enhancing the electrode's specific capacity. In addition, the comparison of the GCD curves of NiCoS@NiCo-LDH, NiCoS, and NiCo-LDH electrodes at a current density of 1 A $g^{-1}$ is shown in Fig. S2.† Fig. 4d illustrates the GCD curves of the NiCoS@NiCo-LDH electrode at various current densities (2–

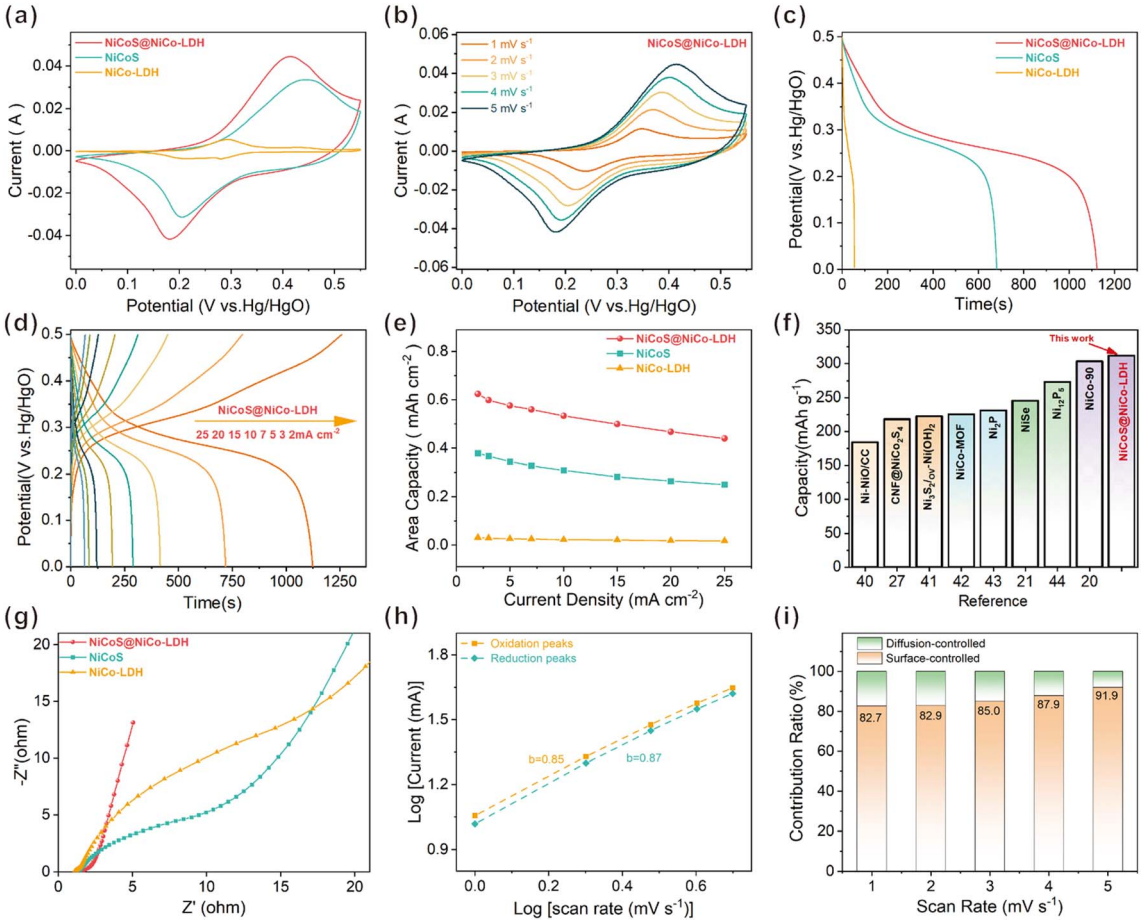


Fig. 4 (a) CV at 5 mV $s^{-1}$ and (c) GCD curves at 2 mA $cm^{-1}$ of the NiCoS@NiCo-LDH, NiCoS, and NiCo-LDH. (b) CV and (d) GCD curves of the NiCoS@NiCo-LDH. (e) Specific capacity of the NiCoS@NiCo-LDH, NiCoS, and NiCo-LDH. (f) Comparison of the capacity of the NiCoS@NiCo-LDH with other reported cathodes for alkaline Zn batteries. (g) Nyquist plots of the NiCoS@NiCo-LDH, NiCoS, and NiCo-LDH. (h) The corresponding *b* values and (i) surface-controlled and diffusion-controlled contributions of the NiCoS@NiCo-LDH.

25 mA cm$^{-2}$), with all curves revealing distinct voltage plateaus. The areal capacities of the NiCoS@NiCo-LDH electrode at current densities of 2, 3, 5, 7, 10, 15, 20, and 25 mA cm$^{-2}$ are respectively 0.624, 0.598, 0.576, 0.56, 0.533, 0.499, 0.467, and 0.44 mA h cm$^{-2}$. Additionally, the CV and GCD curves of the NiCoS and NiCo-LDH electrodes are shown in Fig. S3.† Fig. 4e compares the rate performance of NiCoS@NiCo-LDH, NiCoS, and NiCo-LDH electrodes, where NiCoS@NiCo-LDH exhibits the best rate capability, further underscoring the significant role of the core–shell heterostructure in enhancing specific capacity. As depicted in Fig. 4f, the NiCoS@NiCo-LDH electrode achieves a remarkable specific capacity of 312 mA h g$^{-1}$ at a current density of 2 mA cm$^{-2}$, significantly exceeding many previously reported nickel-based cathode materials such as Ni–NiO/CC (184 mA h g$^{-1}$ at 0.625 A g$^{-1}$),[47] CNF@$NiCo_2S_4$ (218 mA h g$^{-1}$ at 1.26 A g$^{-1}$),[34] $Ni_3S_2/O_V$–$Ni(OH)_2$ (222 mA h g$^{-1}$ at 1 A g$^{-1}$),[48] NiCo-MOF (225 mA h g$^{-1}$ at 1 A g$^{-1}$),[49] $Ni_2P$ (231 mA h g$^{-1}$ at 1 A g$^{-1}$),[50] $NiSe_2$ (243.7 mA h g$^{-1}$ at 1.4 A g$^{-1}$),[25] $Ni_{12}P_5$ (272.8 mA h g$^{-1}$ at 1 A g$^{-1}$),[51] NiCo-90 (303.6 mA h g$^{-1}$ at 2 mA cm$^{-2}$).[24] Furthermore, the EIS reveals the impedance behavior of the electrodes during the electrochemical process. The diameter of the semicircle in the high-frequency region correlates with the charge transfer resistance ($R_{ct}$), reflecting the magnitude of resistance to charge transfer during the electrode reactions.[34] As shown in Fig. 4g, in the high-frequency region, NiCoS@NiCo-LDH exhibits the lowest charge transfer resistance (1.83 Ω), significantly lower than that of NiCoS (6.78 Ω) and NiCo-LDH (11.54 Ω), indicating superior charge transfer capability of the NiCoS@NiCo-LDH electrode. Additionally, the sloping line in the low-frequency region relates to the Warburg diffusion impedance, associated with ion transport within the electrode.[32] The steeper slope in the low-frequency region for NiCoS@NiCo-LDH compared to NiCoS and NiCo-LDH electrodes suggests a more efficient ion transfer capability in the core–shell heterostructure of NiCoS@NiCo-LDH.

The electrode reaction kinetics in the electrochemical process can be elucidated using the following equation:

$$i = av^b \tag{5}$$

Here when the value of $b$ is 0.5 or 1, the electrode reaction is predominantly diffusion-controlled or surface capacitance-controlled, respectively. As shown in Fig. 4h, the $b$ values for the oxidation and reduction peaks of the NiCoS@NiCo-LDH electrode are 0.85 and 0.87, respectively. It suggests that the electrochemical redox processes of the NiCoS@NiCo-LDH electrode involve both surface-controlled and diffusion-controlled processes, with a predominance of surface control. Moreover, the contributions of surface-controlled ($k_1v$) and diffusion-controlled ($k_2v^{1/2}$) processes can be further quantified through the equation:

$$i(V) = k_1v + k_2v^{1/2} \tag{6}$$

where $i(V)$ is the current at a specific potential ($V$).[34] The calculated results, as depicted in Fig. 4i, show the contributions of surface-control processes to the NiCoS@NiCo-LDH electrode are 82.7%, 82.9%, 85.0%, 87.9%, and 91.9% at scan rates of 1, 2, 3, 4, and 5 mV s$^{-1}$, respectively. It indicates that the electrochemical reactions of the NiCoS@NiCo-LDH electrode are mainly governed by surface-control capacitance, which is a critical factor in its outstanding rate performance.

To further evaluate the potential of the NiCoS@NiCo-LDH electrode as a cathode in alkaline batteries, a NiCoS@NiCo-LDH//Zn battery was assembled using a 6 M KOH electrolyte containing saturated ZnO, with NiCoS@NiCo-LDH and zinc foil

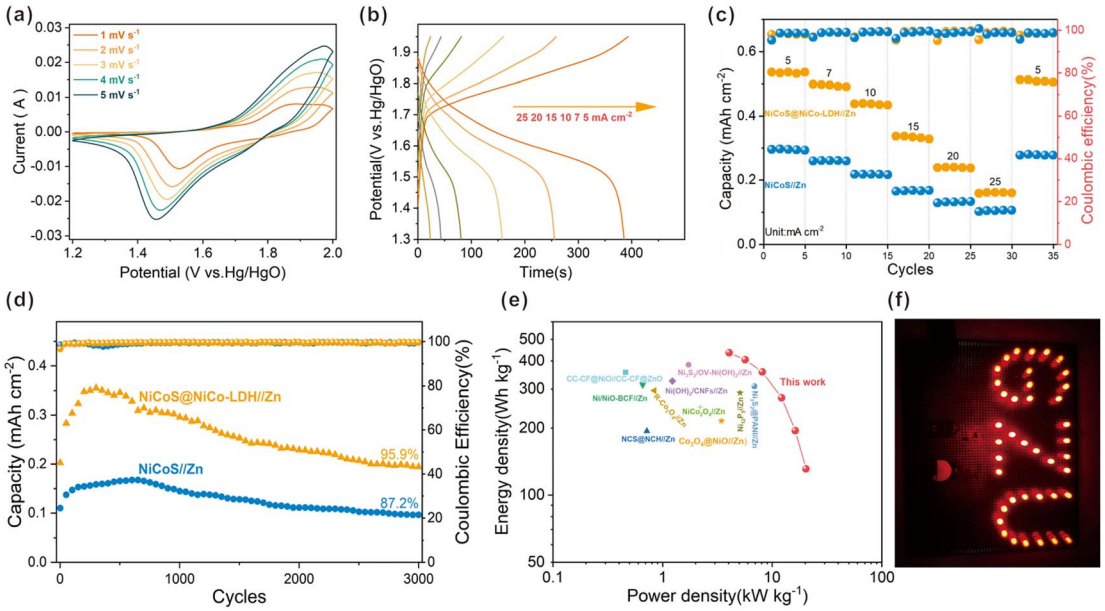


Fig. 5 Electrochemical performance of the NiCoS@NiCo-LDH//Zn and NiCoS//Zn batteries: (a) CV curves at various scan rates, (b) GCD curves for various current densities, (c) rate performance and coulombic efficiency, (d) cyclic stability, and (e) Ragone plots. (f) 40 LEDs powered by NiCoS@NiCo-LDH//Zn.

 

serving as the cathode and anode, respectively. The CV curves of the NiCoS@NiCo-LDH//Zn battery at scan rates of 1–5 mV $s^{-1}$ are shown in Fig. 5a. The CV curves, within the working voltage range of 1.2–2.0 V, exhibit distinct oxidation and reduction peaks at different scan rates, indicating good reversibility of the battery. Fig. 5b presents the galvanostatic charge–discharge (GCD) curves of the NiCoS@NiCo-LDH//Zn battery at various current densities, displaying a discharge voltage plateau at around 1.65 V. As shown in Fig. 5c, the NiCoS@NiCo-LDH//Zn battery demonstrates excellent rate capability and coulombic efficiency. It delivers a reversible areal capacity of 0.54 mA h $cm^{-2}$ at 5 mA $cm^{-2}$ and maintains 0.16 mA h $cm^{-2}$ even at 25 mA $cm^{-2}$. After 30 cycles, it can recover to a reversible capacity of 0.51 mA h $cm^{-2}$ at 5 mA $cm^{-2}$. The outstanding areal-specific capacity is superior to many reported aqueous zinc-based batteries (Table S1†). Moreover, the NiCoS@NiCo-LDH//Zn exhibits improved cycling stability. As illustrated in Fig. 5d, after 3000 cycles at 20 mA $cm^{-2}$, it retains 95.9% of its initial capacity, which is notable compared to most previously studied aqueous zinc-based batteries (Table S2†). Notably, the battery shows a continuous increase in capacity during the first three hundred cycles, which could be attributed to an activation process.

Additionally, Ragone plots comparing the NiCoS@NiCo-LDH//Zn battery with other aqueous zinc-based batteries are presented in Fig. 5e. Thanks to its high capacity and high operating voltage, the fabricated NiCoS@NiCo-LDH//Zn battery achieves a maximum energy density of 435.3 W h $kg^{-1}$ and a power density of 20.3 kW $kg^{-1}$, surpassing many other aqueous zinc-based batteries (Table S3†), such as $Ni_3S_2/O_V$–$Ni(OH)_2$//Zn (384.6 W h $kg^{-1}$ at 1.73 kW $kg^{-1}$),[48] $Ni_{12}P_5$//Zn (287.9 W h $kg^{-1}$ at 5.1 kW $kg^{-1}$),[51] NCS@NCH//Zn (194.2 W h $kg^{-1}$ at 0.72 kW $kg^{-1}$),[52] Ni/NiO-BCF//Zn (313.4 W h $kg^{-1}$ at 0.66 kW $kg^{-1}$),[53] $Ni(OH)_2$/CNFs//Zn (325 W h $kg^{-1}$ at 1.23 kW $kg^{-1}$),[21] R–$Co_3O_4$//Zn (295.5 W h $kg^{-1}$ at 0.84 kW $kg^{-1}$),[54] $NiCo_2O_4$//Zn (248.3 W h $kg^{-1}$ at 2.2 kW $kg^{-1}$),[55] $Ni_3S_2$@PANI//Zn (308 W h $kg^{-1}$ at 6.9 kW $kg^{-1}$),[26] Ni–NiO/CC//Zn (441.7 W h $kg^{-1}$ at 1.1 kW $kg^{-1}$),[47] NiO//ZnO (355.7 W h $kg^{-1}$ at 0.46 kW $kg^{-1}$),[56] $Co_3O_4$@NiO//Zn (215.5 W h $kg^{-1}$ at 3.45 kW $kg^{-1}$).[57] Furthermore, Fig. 5f demonstrates that the NiCoS@NiCo-LDH//Zn battery can power 40 red LEDs, showcasing its significant application potential.

## 4 Conclusion

In summary, we developed a binder-free cathode material comprising NiCoS nanotube@NiCo-LDH nanosheet heterostructures fabricated on nickel foam for efficient AAZBs. The unique three-dimensional core–shell heterostructure exhibits a synergistic effect that enhances conductivity and provides a wealth of active sites and rapid ion/electron transport channels, significantly improving the electrochemical performance. The NiCoS@NiCo-LDH electrode delivers a capacity of 312 mA h $g^{-1}$ (0.624 mA h $cm^{-2}$) at a current density of 2 mA $cm^{-2}$. Furthermore, the fabricated NiCoS@NiCo-LDH//Zn battery achieves a high energy density of 435.3 W h $kg^{-1}$ and maintains 95.9% of its capacity after 3000 cycles at a current density of 20 mA $cm^{-2}$. This work advances the understanding of heterostructured cathode materials and paves the way for developing next-generation high-performance alkaline zinc batteries.

## Author contributions

Linxi Dai conceived the idea, analyzed the study data, and wrote the manuscript. Shangshu Peng performed electrochemical characterization. Xinhai Wang performed SEM and XRD tests. Bo Chen helped analyze the data. Yang Wu helped with the manuscript editing. Quan Xie provided financial support for the project. Yunjun Ruan supervised the study and contributed to the manuscript revision.

## Conflicts of interest

There are no conflicts of interest to declare.

## Acknowledgements

This work was financially supported by the Scientific and Technological Plan Project of Guizhou Province (Grant No. [2021]060), Industry and Education Combination Innovation Platform of Intelligent Manufacturing and Graduate Joint Training Base at Guizhou University (Grant No. 2020-520000-83-01-324061), and Guizhou Engineering Research Center for smart services (Grant No. 2203-520102-04-04-298868). The authors thank Shiyanjia Lab (**https://www.shiyanjia.com**) for XPS and HRTEM tests.

## References

1 S. Lu, W. Yang, M. Zhou, L. Qiu, B. Tao, Q. Zhao, X. Wang, L. Zhang, Q. Xie and Y. Ruan, *J. Colloid Interface Sci.*, 2022, **610**, 1088–1099.
2 S. Peng, Y. Wu, S. Lu, R. Zhao, L. Dai, B. Chen, Q. Xie and Y. Ruan, *Diamond Relat. Mater.*, 2024, **141**, 110646.
3 S. Lu, Q. Xiao, W. Yang, X. Wang, T. Guo, Q. Xie and Y. Ruan, *Int. J. Biol. Macromol.*, 2024, **258**, 128794.
4 D. Chao, W. Zhou, F. Xie, C. Ye, H. Li, M. Jaroniec and S.-Z. Qiao, *Sci. Adv.*, 2020, **6**, eaba4098.
5 K. Shi, W. Yang, Q. Wu, X. Yang, R. Zhao, Z. She, Q. Xie and Y. Ruan, *New J. Chem.*, 2023, **47**, 10153–10161.
6 Q. Wu, T. Guo, Z. Wu, K. Shi, X. Yang, Z. She, R. Zhao and Y. Ruan, *ACS Appl. Nano Mater.*, 2023, **6**, 7456–7464.
7 M. Li, J. Lu, Z. Chen and K. Amine, *Adv. Mater.*, 2018, **30**, 1800561.
8 S. Li, K. Wang, G. Zhang, S. Li, Y. Xu, X. Zhang, X. Zhang, S. Zheng, X. Sun and Y. Ma, *Adv. Funct. Mater.*, 2022, **32**, 2200796.
9 C. D. Quilty, D. Wu, W. Li, D. C. Bock, L. Wang, L. M. Housel, A. Abraham, K. J. Takeuchi, A. C. Marschilok and E. S. Takeuchi, *Chem. Rev.*, 2023, **123**, 1327–1363.
10 X. Jia, C. Liu, Z. G. Neale, J. Yang and G. Cao, *Chem. Rev.*, 2020, **120**, 7795–7866.

11 W. Zhou, D. Zhu, J. He, J. Li, H. Chen, Y. Chen and D. Chao, *Energy Environ. Sci.*, 2020, **13**, 4157–4167.
12 B. Tao, W. Yang, M. Zhou, L. Qiu, S. Lu, X. Wang, Q. Zhao, Q. Xie and Y. Ruan, *J. Colloid Interface Sci.*, 2022, **621**, 139–148.
13 R. Zhao, X. Yang, Z. She, Q. Wu, K. Shi, Q. Xie and Y. Ruan, *Energy Fuels*, 2023, **37**, 3110–3120.
14 L. Qiu, W. Yang, Q. Zhao, S. Lu, X. Wang, M. Zhou, B. Tao, Q. Xie and Y. Ruan, *ACS Appl. Nano Mater.*, 2022, **5**, 6192–6200.
15 W. He, S. Wang, Y. Shao, Z. Kong, H. Tu, Y. Wu and X. Hao, *Adv. Energy Mater.*, 2021, **11**, 2003268.
16 W. Yu, R. Ding, Z. Jia, Y. Li, A. Wang, M. Liu, F. Yang, X. Sun and E. Liu, *Adv. Funct. Mater.*, 2022, **32**, 2112469.
17 B. Zhang, L. Qin, Y. Fang, Y. Chai, X. Xie, B. Lu, S. Liang and J. Zhou, *Sci. Bull.*, 2022, **67**, 955–962.
18 X. Yang, T. Gao, R. Zhao, Q. Wu, K. Shi, Z. She, S. Lu, Q. Xie and Y. Ruan, *Energy Technol.*, 2023, **11**, 2200990.
19 M. Zhou, J. Ma, W. Yang, S. Lu, B. Tao, L. Qiu, X. Wang, Q. Xie and Y. Ruan, *ChemNanoMat*, 2022, **8**, e202200047.
20 C. Xu, J. Liao, C. Yang, R. Wang, D. Wu, P. Zou, Z. Lin, B. Li, F. Kang and C.-P. Wong, *Nano Energy*, 2016, **30**, 900–908.
21 Y. Jian, D. Wang, M. Huang, H.-L. Jia, J. Sun, X. Song and M. Guan, *ACS Sustainable Chem. Eng.*, 2017, **5**, 6827–6834.
22 X. Wang, M. Li, Y. Wang, B. Chen, Y. Zhu and Y. Wu, *J. Mater. Chem. A*, 2015, **3**, 8280–8283.
23 W. Shang, W. Yu, P. Tan, B. Chen, H. Xu and M. Ni, *J. Power Sources*, 2019, **421**, 6–13.
24 H. Chen, Z. Shen, Z. Pan, Z. Kou, X. Liu, H. Zhang, Q. Gu, C. Guan and J. Wang, *Adv. Sci.*, 2019, **6**, 1802002.
25 W. Zhou, J. He, D. Zhu, J. Li and Y. Chen, *ACS Appl. Mater. Interfaces*, 2020, **12**, 34931–34940.
26 L. Zhou, X. Zhang, D. Zheng, W. Xu, J. Liu and X. Lu, *J. Mater. Chem. A*, 2019, **7**, 10629–10635.
27 Z. Sun, Z. Wu, J. Hu, S. Lu, T. Guo, W. Yang, Q. Xie and Y. Ruan, *J. Energy Storage*, 2024, **81**, 110393.
28 J. Hu, Z. Wu, Z. Sun, S. Lu, T. Guo, W. Yang, Q. Xie and Y. Ruan, *ACS Appl. Nano Mater.*, 2024, **7**, 3269–3278.
29 X. Li, Y. Tang, J. Zhu, H. Lv, L. Zhao, W. Wang, C. Zhi and H. Li, *Small*, 2020, **16**, 2001935.
30 L. Zhou, Q. Liu, X. Ma, P. Sun, X. Lv, L. Fang, X. Sun and M.-H. Shang, *Chem. Eng. J.*, 2022, **450**, 138035.
31 Y. Zhang, L. Tao, C. Xie, D. Wang, Y. Zou, R. Chen, Y. Wang, C. Jia and S. Wang, *Adv. Mater.*, 2020, **32**, 1905923.
32 J. Yao, H. Wan, C. Chen, J. Ji, N. Wang, Z. Zheng, J. Duan, X. Wang, G. Ma, L. Tao, H. Wang, J. Zhang and H. Wang, *Nano-Micro Lett.*, 2021, **13**, 167.
33 B. Fei, Z. Yao, D. Cai, J. Si, Q. Wang, Q. Chen, B. Sa, K. Peng and H. Zhan, *Energy Storage Mater.*, 2020, **25**, 105–113.
34 Z. Cui, S. Shen, J. Yu, J. Si, D. Cai and Q. Wang, *Chem. Eng. J.*, 2021, **426**, 130068.
35 Y. Bao, W. Zhang, T. Yun, J. Dai, G. Li, W. Mao, M. Guan and Y. Zhuang, *New J. Chem.*, 2021, **45**, 22491–22496.
36 M. Shi, M. Zhao, L. Jiao, Z. Su, M. Li and X. Song, *J. Power Sources*, 2021, **509**, 230333.
37 W. Wu, C. Zhao, C. Wang, T. Liu, L. Wang and J. Zhu, *Appl. Surf. Sci.*, 2021, **563**, 150324.
38 X. Han, J. Li, J. Lu, S. Luo, J. Wan, B. Li, C. Hu and X. Cheng, *Nano Energy*, 2021, **86**, 106079.
39 Y. U. Jeong and A. Manthiram, *Inorg. Chem.*, 2001, **40**, 73–77.
40 D. Cai, D. Wang, C. Wang, B. Liu, L. Wang, Y. Liu, Q. Li and T. Wang, *Electrochim. Acta*, 2015, **151**, 35–41.
41 C. Xia, P. Li, A. N. Gandi, U. Schwingenschloegl and H. N. Alshareef, *Chem. Mater.*, 2015, **27**, 6482–6485.
42 K. Lin, Z. Zhou, C. Peng, J. Zhang, H. Huang, M. Chen, M. Sun and L. Yu, *Electrochim. Acta*, 2023, **439**, 141546.
43 X. Chen, Y. Wu, Y. Zhou, Z. Xu, C. Wu, L. Li, C. Li, X. Zhang and H. Tong, *Electrochim. Acta*, 2023, **454**, 142376.
44 J. He, X. Shi, Q. Liu, H. Wu, Y. Yu, X. Lu and Z. Yang, *Small*, 2023, **20**, 2306258.
45 D. Shen, M. Li, Y. Liu, X. Fu, H. Yu, W. Dong and S. Yang, *RSC Adv.*, 2023, **13**, 5557–5564.
46 P. Wang, T. Wang, R. Qin, Z. Pu, C. Zhang, J. Zhu, D. Chen, D. Feng, Z. Kou, S. Mu and J. Wang, *Adv. Energy Mater.*, 2022, **12**, 2103359.
47 L. Li, L. Jiang, Y. Qing, Y. Zeng, Z. Zhang, L. Xiao, X. Lu and Y. Wu, *J. Mater. Chem. A*, 2020, **8**, 565–572.
48 X. Wang, Z. Yang, P. Zhang, Y. He, Z.-A. Qiao, X. Zhai and H. Huang, *J. Alloys Compd.*, 2021, **855**, 157488.
49 J. Li, H. Zhao, J. Wang, N. Li, M. Wu, Q. Zhang and Y. Du, *Nano Energy*, 2019, **62**, 876–882.
50 J. Wen, Z. Feng, H. Liu, T. Chen, Y. Yang, S. Li, S. Sheng and G. Fang, *Appl. Surf. Sci.*, 2019, **485**, 462–467.
51 Z. Wang, P. Shi, Q. Liu, J. Li, Y. Gan, J. Yao, J. Xia, X. Liu, X. Chen, K. Qian, X. Liu, L. Lv, G. Ma, L. Tao, J. Zhang, H. Wang, H. Wan and H. Wang, *J. Power Sources*, 2022, **550**, 232170.
52 M. Cui, X. Bai, J. Zhu, C. Han, Y. Huang, L. Kang, C. Zhi and H. Li, *Energy Storage Mater.*, 2021, **36**, 427–434.
53 L. Jiang, L. Li, S. Luo, H. Xu, L. Xia, H. Wang, X. Liu, Y. Wu and Y. Qing, *Nanoscale*, 2020, **12**, 14651–14660.
54 Y. Lu, J. Wang, S. Zeng, L. Zhou, W. Xu, D. Zheng, J. Liu, Y. Zeng and X. Lu, *J. Mater. Chem. A*, 2019, **7**, 21678–21683.
55 H. Z. Zhang, X. Y. Zhang, H. D. Li, Y. F. Zhang, Y. X. Zeng, Y. X. Tong, P. Zhang and X. H. Lu, *Green Energy Environ.*, 2018, **3**, 56–62.
56 J. Liu, C. Guan, C. Zhou, Z. Fan, Q. Ke, G. Zhang, C. Liu and J. Wang, *Adv. Mater.*, 2016, **28**, 8732–8739.
57 Z. Lu, X. Wu, X. Lei, Y. Li and X. Sun, *Inorg. Chem. Front.*, 2015, **2**, 184–187.

 